Chemical Science

ROYAL SOCIETY OF CHEMISTRY

EDGE ARTICLE

View Article Online
View Journal | View Issue

Cite this: *Chem. Sci.*, 2026, **17**, 1792

All publication charges for this article have been paid for by the Royal Society of Chemistry

Organic–inorganic perovskite ferroelectric catalytic selective alkyne coupling under ultrasound sonication

Jun-Chao Qi,† Xiao-Gang Chen, † Zhen-Yu Wang, Yuan-Yuan Tang, Xian-Jiang Song, Yan Qin, Hui-Peng Lv, Ren-Gen Xiong and Wei-Qiang Liao *

Alkyne coupling represents a significant reaction in organic synthesis, while conventional methods rely on high-cost catalysts and harsh reaction conditions. Although ferroelectrics with spontaneous polarization facilitating charge separation have recently attracted great attention as emerging catalysts, their catalytic potential in alkyne coupling remains unexplored. Herein, we report a new organic–inorganic perovskite ferroelectric [4,4-difluoropiperidinium]$_2$-$CuCl_4$ ([DFPD]$_2$-$CuCl_4$), which exhibits a high phase transition temperature of 398 K and room-temperature ferroelectricity. Significantly, by ultrasonic sonication under ambient conditions, and by using [DFPD]$_2$-$CuCl_4$ and additive CuCl as the catalysts, a variety of terminal alkynes can selectively form 1,3-diynes with high yields, with the selectivity and yield up to 99% and 85%, respectively. The high yields enable the growth of crystals of products, three of which exhibit phase transitions. Compared with its inorganic ferroelectric and piezoelectric counterparts, the molecular ferroelectric [DFPD]$_2$-$CuCl_4$ shows significantly enhanced catalytic activity, being approximately 4.5 times that of $BaTiO_3$ and 64 times that of ZnO. Moreover, the [DFPD]$_2$-$CuCl_4$ catalyst demonstrates robust recyclability, with its crystal phase and catalytic activity remaining unchanged over 10 cycles. Our findings provide an efficient and sustainable catalyst system for alkyne coupling and a new perspective on the exploration of ferroelectric catalysis.

Received 8th October 2025
Accepted 17th November 2025

DOI: 10.1039/d5sc07784b

rsc.li/chemical-science

Introduction

Carbon–carbon (C–C) bond formation is of critical importance in organic chemistry.[1] 1,3-Diynes have found widespread applications in synthesizing functional materials, natural products, and pharmaceuticals.[2–6] Compared with the homo-coupling of various alkynyl organometallics, alkynyl tellurides, or alkynyl iodides,[7–9] Glaser coupling—a reaction that constructs C–C bonds *via* terminal alkynes—is widely recognized as the most convenient method for accessing 1,3-diyne products from alkynes in transition metal-catalyzed coupling reactions.[5] Since Glaser first reported in 1869 that the oxidative coupling of copper acetylides could be utilized for diyne synthesis, a diverse range of metal-catalyzed systems has been explored for this reaction, including $CoBr_2$, palladium reagents, $[Ru(dppp)_2(CH_3CN)Cl][BPh_4]$, gold nanoparticles, and Au(I)/Au(III) complexes.[7,10–12] However, their widespread application has been constrained by the high cost of these catalysts or their instability in ambient air. Although significant advances have been made using these approaches, several limitations persist, such as the complex preparation procedures of the catalysts and harsh reaction conditions (*e.g.*, the need for an excess of base or elevated temperatures of 110 °C).[10,13–17] Therefore, there remains an urgent need to develop simpler, more efficient, and environmentally benign methods for the construction of symmetrical 1,3-diyne compounds *via* Glaser coupling.

Ferroelectrics are a significant class of multifunctional electroactive materials with switchable spontaneous polarization, which have been studied for over a century and have found broad applications, such as in data storage, smart sensors, energy conversion, and mechanical actuation.[18–23] In recent years, they have gained increasing attention as emerging catalysts, in which the polarization-induced built-in electric fields and polarization changes under external stimuli such as mechanical stress promote the separation of charge carriers, facilitating redox reactions.[24–37] Their catalytic potentials in hydrogen production, organic synthesis, and environmental remediation under mild conditions of ultrasonic vibration have been intensively studied based on classical ferroelectrics like inorganic $BaTiO_3$ (BTO).[38–49] The inherent polarization electric fields of ferroelectrics also make them attractive for enhancing photocatalytic efficiency through the promotion of photogenerated charge carrier separation and migration dynamics.[35] Molecular ferroelectrics, as represented by $[Me_3NCH_2Cl]CdCl_3$,

Ordered Matter Science Research Center, Nanchang University, Nanchang, 330031, People's Republic of China. E-mail: liaowq@ncu.edu.cn

† The authors contributed equally to this work.

are ferroelectric materials with molecular constituents in their crystal lattices in which the ferroelectricity is related to the collective interactions and arrangements of the molecular components.[50] Compared with the widely used atom-based inorganic ferroelectrics with rigid ionic/covalent bonds throughout the lattices, molecular ferroelectrics constructed from molecular constituents with intermolecular interactions (*e.g.*, hydrogen bonds and van der Waals forces) possess many advantages and distinct properties, such as low-temperature solution processability, light weight, mechanical flexibility, lower acoustic impedance, bio-compatibility, chemical tunability, homochirality, and photoisomerization.[50–63] Notably, the low acoustic impedance of molecular ferroelectrics can facilitate the mechanical energy transfer from solvent to catalysts, and their solvent solubility enables good catalyst recyclability, rendering them highly promising for efficient and sustainable ferroelectric catalysis under mild conditions.[64–70] Among molecular ferroelectrics, organic–inorganic metal halide perovskite ferroelectrics represent a synergistic integration of structural and functional merits,[50] such as the coexistence of ferroelectric and magnetic orders in copper(II)-based halide perovskite ferroelectrics.[71–73] Nevertheless, molecular ferroelectric catalysis remains in its infancy, and ferroelectric catalytic alkyne coupling has never been explored.

Herein, we demonstrated a new Cu^{2+}-based organic–inorganic perovskite ferroelectric [4,4-difluoropiperidinium]$_2$-$CuCl_4$ ([DFPD]$_2$-$CuCl_4$), which shows a high phase transition temperature of 398 K and room-temperature ferroelectricity. Significantly, by using molecular ferroelectric [DFPD]$_2$-$CuCl_4$ with the addition of CuCl as a catalyst, we achieved efficient construction of 1,3-diynes *via* terminal alkyne homocoupling under ultrasonic irradiation. Traditional methods typically require pre-functionalization, noble metal catalysts, an excess of base, or high temperature (Scheme 1a).[7–17] This catalytic system exhibits several advantages, such as mild reaction conditions, high selectivity, and good yield (maximum 88%) (Scheme 1b). Furthermore, the molecular ferroelectric catalysts demonstrate robust recyclability, with their crystalline structure and catalytic activity remaining unchanged over multiple cycles—aligning with green chemistry principles. Moreover, the catalytic performance of the molecular ferroelectric [DFPD]$_2$-$CuCl_4$ with CuCl is significantly superior to that of inorganic ferroelectrics and piezoelectric materials with CuCl, that is, approximately 4.5 times that of $BaTiO_3$ and 64 times that of ZnO (Scheme 1c). This work opens up a new avenue for catalytic alkyne coupling and provides a new perspective on the exploration of ferroelectric catalysis.

Results and discussion

Crystal structures and phase transitions

We prepared [DFPD]$_2$-$CuCl_4$ as crystals by evaporating stoichiometric amounts of 4,4-difluoropiperidine hydrochloride and copper dichloride in a hydrochloric acid solution at 323 K. Powder X-ray diffraction (PXRD) patterns of as-grown crystals match the simulated patterns, revealing the good phase purity of [DFPD]$_2$-$CuCl_4$ (Fig. S1). The thermogravimetric analysis (TGA) curve of [DFPD]$_2$-$CuCl_4$ demonstrates thermal stability up to about 512 K (Fig. S2). Single-crystal structure determination reveals that [DFPD]$_2$-$CuCl_4$ crystalizes in a non-centrosymmetric orthorhombic space group $Cmc2_1$ with a polar point group of $mm2$ at 300 K (Table S1), which is consistent with the previous report of the polar structure of [DFPD]$_2$-$CuCl_4$ by L.-N. Quan and co-workers.[74] As shown in Fig. 1a and S3, [DFPD]$_2$-$CuCl_4$ adopts an A_2BX_4-type organic–inorganic perovskite structure, in which the two organic $DFPD^+$ cationic layers alternate with the inorganic anionic $CuCl_4^{2-}$ framework. The presence of N–H···Cl hydrogen bonds between inorganic anions and organic cations with donor–acceptor distances of 3.269(3)–3.408(3) Å (Table S2) not only stabilizes the structure of [DFPD]$_2$-$CuCl_4$ but also promotes the ordered arrangement of $DFPD^+$ cations along the *c*-axis, thereby inducing spontaneous polarization in this

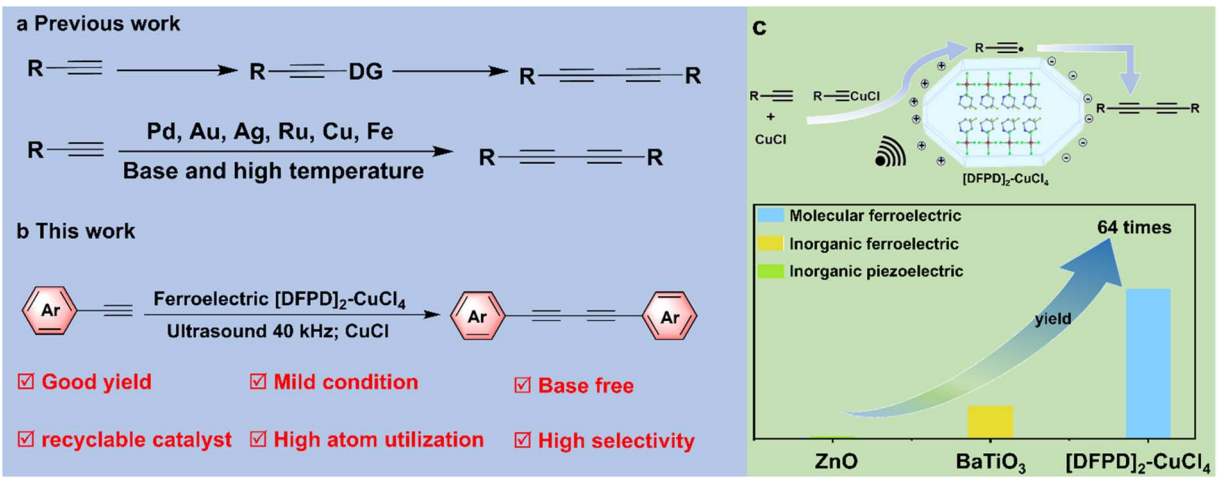

Scheme 1 (a) Survey of classic synthesis pathways. (b) Our strategy of molecular ferroelectric-catalyzed alkyne coupling. (c) Diagram of the proposed ferroelectric catalytic mechanism and comparison of catalytic activity by using molecular ferroelectric [DFPD]$_2$-$CuCl_4$, traditional inorganic ferroelectric $BaTiO_3$, and inorganic piezoelectric ZnO.

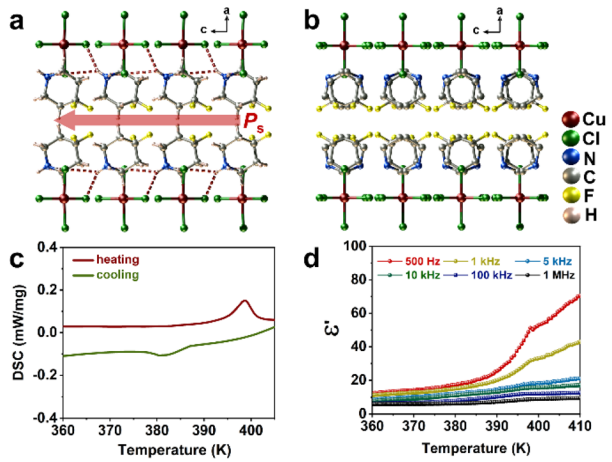

Fig. 1 (a and b) Packing view of the crystal structure of $[DFPD]_2$-$CuCl_4$ at (a) 300 K and (b) 410 K. (c) DSC curves of $[DFPD]_2$-$CuCl_4$ upon heating and cooling runs. (d) Real part (ε') of the dielectric constant of $[DFPD]_2$-$CuCl_4$ at different frequencies as a function of temperature. The red arrow represents the direction of spontaneous polarization. The red dotted line indicates N–H···Cl hydrogen bonds. Hydrogen atoms of the disordered DFPD cations at 410 K are omitted for clarity.

direction. At 410 K, the space group transitions to the centrosymmetric space group *Cmcm* with the point group *mmm*. At this point, the $DFPD^+$ cations are located precisely at special symmetric sites on the mirror plane, changing from the initial ordered state to a two-fold disordered state, resulting in the cancellation of polarization (Fig. 1b), which is distinct from the displacive-type mechanism prevalent in inorganic ferroelectrics. According to the 88 types of ferroelectric phase transitions,[20] $[DFPD]_2$-$CuCl_4$ undergoes a *mmmFmm*2-type ferroelectric–paraelectric phase transition.

The variable-temperature PXRD patterns show that as the temperature increases, the peak positions exhibit a distinct shift to lower angles, indicating an increase in the 2D interlayer spacing (Fig. S4). Furthermore, the diffraction peak at around 23° at 410 K undergoes a significant change, providing further evidence of a structural phase transition. This structural phase transition was subsequently accurately confirmed by differential scanning calorimetry testing, with the Curie temperature (T_c) during the heating process being 398 K (Fig. 1c). The non-centrosymmetric to centrosymmetric transition of $[DFPD]_2$-$CuCl_4$ was further demonstrated by second-harmonic generation (SHG) spectroscopy. As the temperature increased to 410 K, the SHG signal vanished, consistent with the structural phase transition from non-centrosymmetric space group $Cmc2_1$ to centrosymmetric space group *Cmcm*. The SHG activity can be recovered when the crystal is cooled to 300 K, implying the reversibility of the phase transition (Fig. S5). As shown in Fig. 1d, the pronounced anomaly in the real part (ε') of the dielectric constant near T_c further confirms the occurrence of the ferroelectric–paraelectric phase transition. The non-centrosymmetric crystal symmetry also indicates that $[DFPD]_2$-$CuCl_4$ has a piezoelectric response. We then measured its piezoelectric coefficient d_{33}, one of the most useful piezoelectric coefficients, *via* the quasi-static method (Berlincourt method) on single crystals. A d_{33} value of 12 pC/N was obtained (Fig. S6).

Ferroelectricity

The polar point group *mm*2 of $[DFPD]_2$-$CuCl_4$ belongs to one of ten polar point groups for ferroelectrics. We then detected the ferroelectricity of $[DFPD]_2$-$CuCl_4$ by piezoresponse force microscopy (PFM), which is a promising technique for characterizing micro- to nanoscale structures, enabling direct probing and visualization of ferroelectric domain configurations. In the amplitude and phase images generated by PFM, distinct colors are employed to represent the local piezoelectric response and the polarization orientation of the material, respectively. To confirm the ferroelectric properties of $[DFPD]_2$-$CuCl_4$, PFM analysis was performed on its thin film, as shown in Fig. 2 and 3. The phase image reveals an approximate 180° contrast difference between two regions of distinct colors (Fig. 2a), indicating opposing polarization directions in these areas. In the amplitude image (Fig. 2b), the boundaries between these two regions exhibit a significant reduction in signal intensity, clearly indicating the locations of the domain walls. Moreover, the PFM signals appear to be independent of surface morphological features (Fig. 2c), thereby ruling out the influence of surface topography and further confirming the presence of ferroelectric domains. Meanwhile, switching measurements were conducted to verify the polarization reversal phenomenon in the film under the application of an electric field. As shown in Fig. 2d, the phase–bias curves display a clear hysteresis loop, and the amplitude–bias curves exhibit a characteristic butterfly-shaped pattern, demonstrating the domain switching.

We also conducted domain switching measurements to directly visualize the polarization reversal behavior (Fig. 3). We initially select a single domain to serve as the starting state

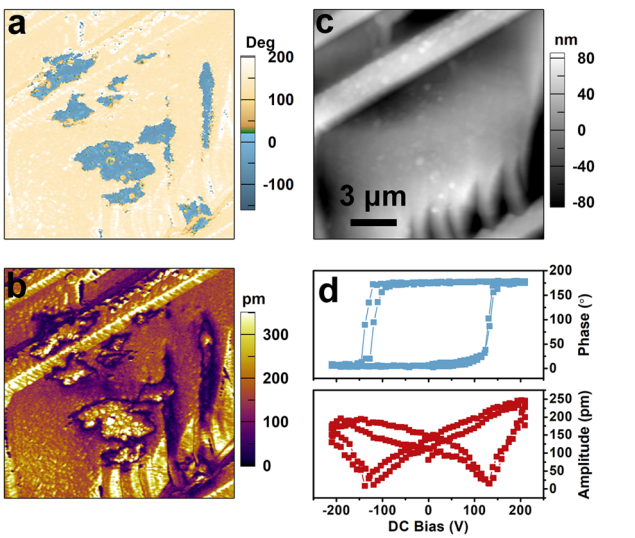

Fig. 2 PFM (a) phase and (b) amplitude, and corresponding (c) topographic images on the film of $[DFPD]_2$-$CuCl_4$. (d) Local PFM hysteresis loops obtained by plotting the phase and amplitude signals as functions of the tip voltage for a selected point.

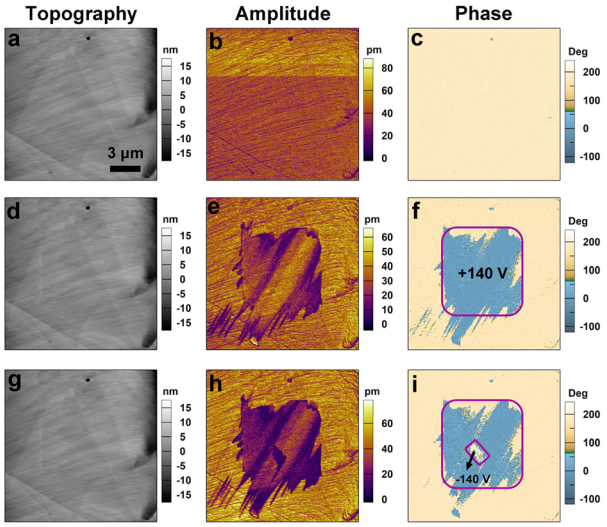

Fig. 3 Ferroelectric domain switching for $[DFPD]_2$-$CuCl_4$. Topography (a, d and g), PFM amplitude (b, e and h), and phase (c, f and i) images were taken in the as-grown state (a–c), after applying a tip voltage of +140 V in the central region (d–f), and after applying an opposite tip voltage of −140 V in a smaller region.

(Fig. 3a–c). Subsequently, a +140 V voltage was applied to the central region (Fig. 3d–f). It can be observed from Fig. 3f that a new color contrast emerges in the phase diagram, differing from the original by nearly 180°, which indicates the formation of a new domain. Furthermore, an opposite tip voltage of −140 V was applied to a smaller region within the newly formed domain, resulting in partial back-switching of the domain (Fig. 3g–i). These observations provide strong evidence for polarization switching occurring within the ferroelectric domains of compound $[DFPD]_2$-$CuCl_4$.

Ferroelectric catalysis

We next investigated the catalytic activity of $[DFPD]_2$-$CuCl_4$ in alkyne coupling reactions. Initially, the reaction was conducted using 1 mmol of phenylacetylene as the substrate, $[DFPD]_2$-$CuCl_4$ crystals as the catalyst, CuCl as the additive, and acetonitrile (MeCN) as the solvent, with ultrasonic irradiation at 40 kHz for 6 hours (Fig. 4 and 5). Following purification by column chromatography, product **2a** was obtained in 64% yield. Notably, colorless and transparent crystals of **2a** were further isolated *via* slow evaporation of the reaction solution in *n*-hexane (Fig. 5). Subsequently, the role of each catalytic component was examined (Fig. 4a and Table S3). In the absence of $[DFPD]_2$-$CuCl_4$, no **2a** was detected; similarly, omitting CuCl also resulted in no formation of **2a**. These results confirm that the reaction proceeds *via* the co-catalysis of $[DFPD]_2$-$CuCl_4$ and CuCl, in which CuCl reacts with phenylacetylene to form a cuprous phenylethynide intermediate,[16,17] while the release of free charges from the surface of the $[DFPD]_2$-$CuCl_4$ ferroelectric catalyst under ultrasonic stimulation facilitates the conversion of the cuprous phenylethynide intermediate to the alkyne coupling product. We also evaluated the effect of ultrasound on reaction efficiency by testing the yield in the absence of ultrasonic irradiation. Only 12% of **2a** was obtained under non-ultrasonic conditions, which is significantly lower than that achieved with ultrasound—clearly indicating that ultrasound promotes reaction progression. Next, the influence of different catalysts on the reaction was investigated (Fig. 4b and Table S4). When sodium chloride (NaCl), a centrosymmetric crystal with neither ferroelectric nor piezoelectric properties, was used as the catalyst; no **2a** was detected. Employing piezoelectric ZnO crystals as the catalyst only yielded trace amounts of **2a** (≈1%). Replacing $[DFPD]_2$-$CuCl_4$ with BTO afforded **2a** in a 14% yield. Although both ZnO and BTO were capable of promoting product formation, their catalytic activities were substantially lower than that of $[DFPD]_2$-$CuCl_4$: specifically, the catalytic activity of $[DFPD]_2$-$CuCl_4$ is approximately 64 times that of ZnO and 4.5 times that of BTO. This reaction was also carried out using the non-ferroelectric centrosymmetric Cu^{2+}-based organic–inorganic hybrid perovskite $[cyclobutylammonium]_2$-$CuCl_4$ ($[CBA]_2$-$CuCl_4$)[65] as the catalyst. Under standard conditions, product **2a** was obtained with a yield of only 13% (Fig. 4b and Table S4), which is significantly lower than that achieved when $[DFPD]_2$-$CuCl_4$ is used as the catalyst. This further demonstrates the essential role of molecular ferroelectrics in catalysis. Finally, the impact of different Cu^+ sources was explored. When CuBr or CuI was used instead of CuCl, the yield of **2a** decreased: CuCl afforded the highest yield (64%), whereas CuBr and CuI gave yields of 40% and 44%, respectively (Table S5). Based on the control experiment, a possible mechanism has been proposed. CuCl first reacts with phenylacetylene to form a cuprous phenylethynide intermediate. Under ultrasonic stimulation, free charges of electron–hole pairs are released from the molecular ferroelectric $[DFPD]_2$-$CuCl_4$ crystal surface. This facilitates the cuprous phenylethynide intermediate to lose an electron to form a phenylethynyl radical. Subsequently, the phenylethynyl radicals couple to generate product **2a**.

After optimizing the reaction conditions, we next investigated the recyclability of the $[DFPD]_2$-$CuCl_4$ catalyst. Following reaction completion, the solid $[DFPD]_2$-$CuCl_4$ catalyst was recovered *via* filtration and reused in subsequent cycles. Notably, the catalyst maintained consistent catalytic activity, yield, and selectivity over 10 consecutive cycles (Fig. 4c), confirming its good recyclability. As shown in Fig. 4d, the PXRD patterns of $[DFPD]_2$-$CuCl_4$ after 10 cycles of use are consistent with the original ones, indicating a stable crystal phase during the reaction. We also investigated the piezoelectric properties of the recycled catalyst (Fig. 4e and f). Since the samples were polycrystalline, we selected points from the PFM mapping that exhibited the highest amplitude signals for resonant measurements, using a driving voltage of 2 V. By sweeping the AC voltage frequency, typical resonant peaks in the amplitude response were observed, as shown in Fig. 4e. These curves were well fitted by a simple harmonic oscillator (SHO) model. Based on the resonance peaks, no significant variation was observed in the piezoresponse of the catalyst before cycling and after 10 cycles of recycling. From the SHO fitting, we extracted the quality factor, which reflects the degree of amplitude signal amplification. Dividing the measured amplitude signal by the quality factor yields the intrinsic amplitude signal, which is expected to

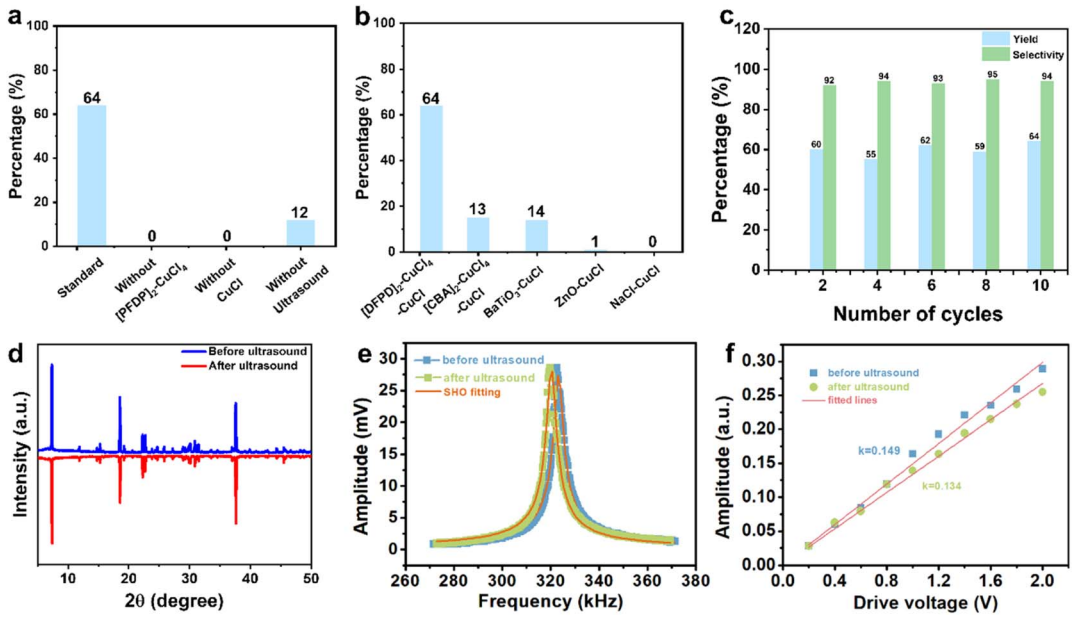

Fig. 4 (a) Control experiments of the influence of conditions on the reaction. (b) The effects of different catalysts on experiments. (c) Ferroelectric catalyst-recycling experiments. (d) PXRD patterns of initial and after 10 cycles recycled $[DFPD]_2$-$CuCl_4$. (e) Measured amplitude *versus* drive frequency analyzed by the SHO model for the pressed pellet samples of initial and after 10 cycles recycled $[DFPD]_2$-$CuCl_4$. (f) Intrinsic amplitude *versus* drive voltage for the pressed pellet samples of initial and after 10 cycles recycled $[DFPD]_2$-$CuCl_4$.

be linearly proportional to the applied driving voltage, as illustrated in Fig. 4f. The slopes of these curves represent the magnitude of the piezoelectric response, confirming that the detected signals originate from the intrinsic piezoelectric effect. This further demonstrates that the piezoelectric properties of $[DFPD]_2$-$CuCl_4$ remain stable after 10 cycles of use.

Subsequently, the substrate scope of this molecular ferroelectric-catalyzed coupling of terminal alkynes has been evaluated (Fig. 5). First, a wide range of alkynes with electron-donating groups was investigated. Phenylacetylenes substituted with either a *tert*-butyl group (**2b**) or a methyl group (**2c**) at the *para* position are compatible with this strategy, and the corresponding products can be obtained in good yields of 70% and

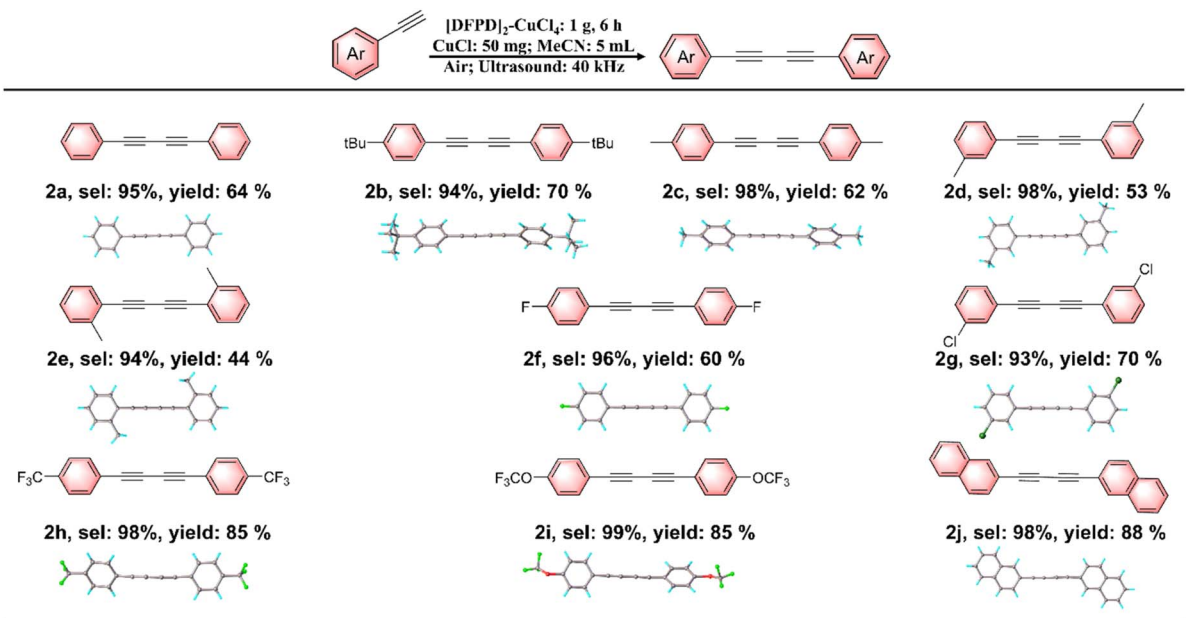

Fig. 5 Reactions were carried out on 1 mmol terminal alkynes, $[DFPD]_2$-$CuCl_4$ (1 g), and CuCl (50 mg) in MeCN (5 mL) under a 40 kHz ultrasound condition for 6 h. The single crystal structures of all products are placed below the corresponding structural formulae.

62% with a selectivity of 94% and 98%, respectively. We further investigated the effect of electron-donating groups at different positions on the reaction efficiency, and found that phenylacetylenes with methyl substituents at the *ortho* and *meta* positions both exhibited a significant decrease in yield. Additionally, we explored the substrate scope of alkynes containing electron-withdrawing groups. Both 4-fluorophenylacetylene and 3-chlorophenylacetylene were able to generate the corresponding products in good yields of 60% and 70% with an excellent selectivity of 96% and 93% respectively. Notably, 4-trifluoromethylphenylethyne and 4-trifluoromethoxyphenylethyne—bearing strong electron-withdrawing groups—exhibit not only excellent compatibility with this protocol but also afford the corresponding products in outstanding yields of 85% and 85% with an excellent selectivity of 98% and 99% respectively. In addition to phenylacetyne derivatives, we also explored other aryl-acetylenes. 2-Ethynylnaphthalene was also applicable to this protocol, providing the corresponding product in an excellent yield of 88% with an excellent selectivity of 98%. These results demonstrate that the current protocol has excellent substrate generality, suggesting great potential for practical applications. The structures of the target products were demonstrated by nuclear magnetic resonance (NMR) spectroscopy and single-crystal XRD (Fig. S7–S38).

The high yield of obtained products enables them to yield the corresponding crystals through slow crystallization in *n*-hexane (Fig. 6, S30–S38, Tables S6 and S7). Notably, in these products, **2f**, **2i**, and **2j** exhibit phase transition behavior (Fig. 6a, S35, and S38). As shown in Fig. 6a, DSC analyses indicate that compound **2i** exhibits two pairs of reversible phase transitions with transition temperatures of $T_{c1} = 271$ K and $T_{c2} = 195$ K, respectively. The temperature-dependent real part ε' of the dielectric constant shows anomalies near the two phase transition temperatures (Fig. 6b), further confirming the phase transition. The variable-temperature single-crystal XRD measurements of compound **2i** show that it crystallized in the centrosymmetric space group $P\bar{1}$ at 300 K. When cooling to the intermediate-temperature phase at 193 K and the low-temperature phase at 173 K, the space groups remain $P\bar{1}$, while the cell volume reduces to approximately 1/4 and 1/2 that of the room-temperature phase, respectively (Table S7). As Fig. 6c shows, the change in the dihedral angle of two benzene rings in the **2i** molecule is responsible for the phase transitions.

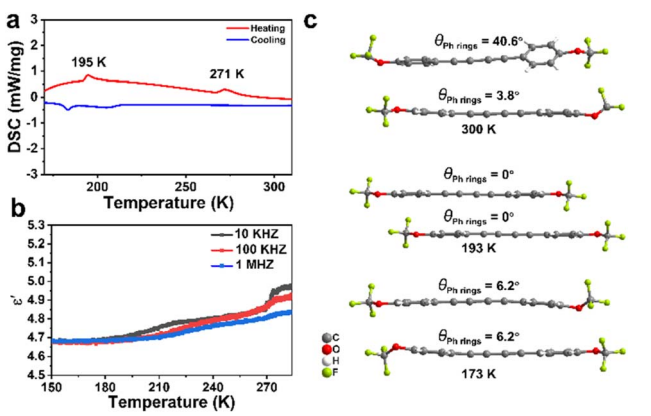

Fig. 6 (a) DSC curves and (b) the temperature-dependent dielectric real part (ε') of compound **2i**. (c) Crystal structure of compound **2i** at 300 K, 193 K, and 173 K, respectively, showing the change in the dihedral angle of two benzene rings ($\theta_{Ph\ rings}$) in the **2i** molecule.

Conclusions

In summary, we demonstrated a Cu^{2+}-based new organic–inorganic perovskite ferroelectric $[DFPD]_2$-$CuCl_4$ and its excellent catalytic activity in alkyne coupling. $[DFPD]_2$-$CuCl_4$ shows a high phase transition temperature of 398 K and room-temperature ferroelectricity. Under ultrasonic vibration, with $[DFPD]_2$-$CuCl_4$ and CuCl as the catalysts, a variety of terminal alkynes can selectively form 1,3-diynes with high yields. Specifically, for the electron-deficient alkyne (4-trifluoromethylphenylacetylene), the selectivity and yield reach up to 99% and 85%, respectively. Compared with inorganic ferroelectrics and piezoelectrics with CuCl, the molecular ferroelectric $[DFPD]_2$-$CuCl_4$ shows significantly enhanced catalytic activity, being approximately 4.5 times that of $BaTiO_3$ and 64 times that of ZnO. Moreover, the molecular ferroelectric catalysts demonstrate robust recyclability, with their crystalline structure and catalytic activity remaining unchanged over multiple cycles. This work develops an efficient and sustainable catalyst system for alkyne coupling. It also advances the fundamental understanding of ferroelectric catalysis, paving the way for next-generation catalytic technologies in fine chemical synthesis and materials engineering.

Experimental

Synthesis and growth of crystals

Materials were obtained from commercial suppliers and purified by standard procedures unless otherwise noted. Solvents for reactions were purchased from commercial suppliers. The molecular ferroelectric crystal $[DFPD]_2$-$CuCl_4$ was obtained using the following method. 4,4-Difluoropiperidine hydrochloride (20 mmol) and $CuCl_2$ (10 mmol) were dissolved in hydrochloric acid to get a clear solution. Slow evaporation of solvent at 323 K results in the $[DFPD]_2$-$CuCl_4$ crystals.

For the catalytic reaction, the $[DFPD]_2$-$CuCl_4$ crystals (1 g) were first ground into powder. Then, in a sealed tube, 1 mmol of phenylacetylene, 1 g of powder $[DFPD]_2$-$CuCl_4$, and 0.05 g CuCl were placed in 5 mL MeCN. The reaction was then placed in an ultrasonic environment with a frequency of 40 kHz for 6 h. During the experiment, circulating water was used. The organic layer was collected, dried over sodium sulfate, filtered, and concentrated. The crude product was subsequently purified by column chromatography on silica gel (200–300 meshes) using a mixture of PE/EA (20 : 1) as the eluent. Slow evaporation of the *n*-hexane solution of the obtained products yields the corresponding crystals.

Characterization

Methods for powder and single-crystal XRD, TGA, DSC, dielectric constant, SHG, PFM, and NMR measurements were described in the SI.

Author contributions

W.-Q. L. and R.-G. X. devised and developed the project. J.-C. Q. and X.-G. C. contributed equally to this work. J.-C. Q. synthesized the samples and carried out the catalytic experiments. X.-G. C. conducted XRD, DSC, and dielectric measurements. Y. Q. performed SHG measurements. Z.-Y. W. performed crystal structure analysis. H.-P. L. performed the d_{33} measurement. Y.-Y. T. and X.-J. S. performed PFM experiments. All the authors analyzed the data, discussed the results and contributed to the manuscript.

Conflicts of interest

There are no conflicts to declare.

Data availability

The data supporting this article have been included as part of the supplementary information (SI). Supplementary information is available. See DOI: https://doi.org/10.1039/d5sc07784b.

CCDC 2484549, 2484550, 2484236–2484244, and 2484246–2484250, respectively contain the supplementary crystallographic data for this paper.[75a–p]

Acknowledgements

This work was supported by the National Key R&D Program of China (2024YFA1509300) and the National Natural Science Foundation of China (22488101, 22175082, 22201120, and 22401132).

Notes and references

1 Y. Zhou and J. Zhao, *Appl. Catal., B.*, 2022, **300**, 120721.
2 J.-Q. Li, Z.-Q. Xie, Y. Xiong, Z.-Z. Li, Q.-X. Huang, S.-Q. Zhang, J.-Y. Zhou, R. Liu, X. Gao, C.-G. Chen, L.-M. Tong, J. Zhang and Z.-F. Liu, *Adv. Mater.*, 2017, **29**, 1700421.
3 S. Eisler, A.-D. Slepkov, E. Elliott, T. Luu, R. McDonald, F.-A. Hegmann and R.-R. Tykwinski, *J. Am. Chem. Soc.*, 2005, **127**, 2666–2676.
4 B. Zhang, Y. Wang, S.-P. Yang, Y. Zhou, W.-B. Wu, W. Tang, J.-P. Zuo, Y. Li and J.-M. Yue, *J. Am. Chem. Soc.*, 2012, **134**, 20605–20608.
5 J.-Z. Liu, J.-W.-Y. Lam and B.-Z. Tang, *Chem. Rev.*, 2009, **109**, 5799–5867.
6 B. Saikia, T.-J. Devi and N.-C. Barua, *Org. Biomol. Chem.*, 2013, **11**, 23189–23193.
7 F. Albrecht, D. Rey, S. Fatayer, F. Schulz, D. Pérez, D. Peña and L. Gross, *Angew. Chem., Int. Ed.*, 2020, **59**, 1780–1787.
8 Y. Nishihara, K. Ikegashira, K. Hirabayashi, J. -I Ando, A. Mori and T. Hiyama, *J. Org. Chem.*, 2000, **65**, 1780.
9 H.-H. Kong, L. Viergutz, L.-C. Liu, A. Sandvoß, X.-C. Peng, H.-N. Klaasen, H. Fuchs and A. Studer, *Adv. Mater.*, 2023, **35**, 2210997.
10 H.-Y. Gao, H. Wagner, D.-Y. Zhong, J.-H. Franke, A. Studer and H. Fuchs, *Angew. Chem., Int. Ed.*, 2013, **52**, 4024–4028.
11 W. Shi, Y.-D. Luo, X.-C. Luo, L. Chao, H. Zhang, J. Wang and A.-W. Lei, *J. Am. Chem. Soc.*, 2008, **130**, 14713–14720.
12 A. Leyva-Pérez, A. Doménech-Carbó and A. Corma, *Nat. Commun.*, 2015, **6**, 6703.
13 H. Plenio, *Angew. Chem.*, 2008, **120**, 7060–7063.
14 P. Kuhn, A. Alix, M. Kumarraja, B. Louis, P. Pale and J. Sommer, *Eur. J. Org. Chem.*, 2009, **3**, 423–429.
15 O. Vechorkin, D. Barmaz, V. Proust and X.-L. Hu, *J. Am. Chem. Soc.*, 2009, **131**, 12078–12079.
16 L.-B. Su, J.-Y. Dong, L. Liu, M.-L. Sun, R.-H. Qiu, Y.-B. Zhou and S.-F. Yin, *J. Am. Chem. Soc.*, 2016, **138**, 12348–12351.
17 Z.-H. Zhang, X.-Y. Dong, X.-Y. Du, Q.-S. Gu and X.-Y. Liu, *Nat. Commun.*, 2019, **10**, 5689.
18 J. F. Scott, *Science*, 2007, **315**, 954–959.
19 M. E. Lines and A. M. Glass, *Principles and Applications of Ferroelectrics and Related Materials*, Oxford University Press, Oxford, 2001.
20 H. Peng, J.-C. Qi, Y.-S. Liu, J.-M. Zhang, W.-Q. Liao and R.-G. Xiong, *Chin. J. Chem.*, 2024, **42**, 1133–1144.
21 J.-C. Qi, Y. Qin, H. Peng, H.-P. Lv, Y.-J. Bai, X. Shen, Z.-T. Xia and W.-Q. Liao, *Sci. China: Chem.*, 2024, **67**, 4167–4174.
22 F. Wang, L. Ju, B. Wu, S. Li, J. Peng, Y. Chen, M. G. Sendeku, K. Wang, Y. Cai, J. Yi, Y. Yang, Z. Wang and X. Sun, *Angew. Chem., Int. Ed.*, 2024, **63**, e202402033.
23 C.-F. Wang, Y. Yang, Y. Hu, C. Ma, H.-F. Ni, P.-G. Liu, H.-F. Lu, Z.-X. Zhang, J.-G. Wang, Y.-J. Zhang, D.-W. Fu, K. Zhao and Y. Zhang, *Angew. Chem., Int. Ed.*, 2024, **63**, e202413726.
24 T. Choi, S. Lee, Y. J. Choi, V. Kiryukhin and S. W. Cheong, *Science*, 2009, **324**, 63–66.
25 X.-L. Xu, L.-B. Xiao, J. Zhao, B.-K. Pan, J. Li, W.-Q. Liao, R.-G. Xiong and G.-F. Zou, *Angew. Chem., Int. Ed.*, 2020, **59**, 20149–20157.
26 Y. Liu, S. Ye, H. Xie, J. Zhu, Q. Shi, N. Ta, R. Chen, Y. Gao, H. An, W. Nie, H. Jing, F. Fan and C. Li, *Adv. Mater.*, 2020, **32**, 1906513.
27 Y. Du, X. Zhao, F. He, H. Gong, J. Yang, L. Wu, X. Cui, S. Gai, P. Yang and J. Lin, *Adv. Mater.*, 2024, **36**, 2403253.
28 M. M. Yang and M. Alexe, *Adv. Mater.*, 2018, **30**, 1704908.
29 H. You, Z. Wu, L. Zhang, Y. Ying, Y. Liu, L. Fei, X. Chen, Y. Jia, Y. Wang, F. Wang, S. Ju, J. Qiao, C.-H. Lam and H. Huang, *Angew. Chem., Int. Ed.*, 2019, **58**, 11905–11910.
30 S. Li, Z. Zhao, J. Zhao, Z. Zhang, X. Li and J. Zhang, *Appl. Nano Mater.*, 2020, **3**, 1063–1079.
31 J. Huang, Y. Kang, J. Liu, T. Yao, J. Qiu, P. Du, B. Huang, W. Hu, Y. Liang, T. Xie, C. Chen, L.-C. Yin, L. Wang, H.-M. Cheng and G. Liu, *Nat. Commun.*, 2023, **14**, 7948.
32 L. Ju, Y. Ma, X. Tan and L. Kou, *J. Am. Chem. Soc.*, 2023, **145**, 26393–26402.
33 S.-L. Niu, W. Yuan, X. Gong, B. Bao, Z.-W. Wu, B. Xu, R. Zeng, Q.-W. Yang and Q. Ouyang, *ACS Sustainable Chem. Eng.*, 2023, **11**, 17816–17825.
34 X. Liao, H. Xie, B. Liao, S. Hou, Y. Yu and X. Fan, *Nano Energy*, 2022, **94**, 106890.
35 G. Wan, L. Yin, X. Chen, X. Xu, J. Huang, C. Zhen, H. Zhu, B. Huang, W. Hu, Z. Ren, H. Tian, L. Wang, G. Liu and H.-M. Cheng, *J. Am. Chem. Soc.*, 2022, **144**, 20342–20350.

36 Z. Wang, J. Wang, J. Ayarza, T. Steeves, Z.-Y. Hu, S. Manna and A.-P. Esser-Kahn, *Nat. Mater.*, 2021, **20**, 869–874.
37 C. Schumacher, J. G. Hernández and C. Bolm, *Angew. Chem., Int. Ed.*, 2020, **59**, 16357–16360.
38 D.-X. Zhou, Z. Li, Y. Chen, H.-H. Dong, Y.-Y. Zhou, Z.-F. Bian and M.-S. Zhu, *Angew. Chem., Int. Ed.*, 2025, **64**, e202502751.
39 S. Tu, Y. Guo, Y. Zhang, C. Hu, T. Zhang, T. Ma and H. Huang, *Adv. Funct. Mater.*, 2020, **30**, 2005158.
40 K. Wang, C. Han, J.-Q. Li, J.-S. Qiu, J. Sunarso and S.-M. Liu, *Angew. Chem., Int. Ed.*, 2022, **61**, e202110429.
41 Z.-Y. Ren, Y.-H. Peng, H.-L. He, C.-H. Ding, J.-L. Wang, Z. Wang and Z.-B. Zhang, *Chin. J. Chem.*, 2023, **41**, 111–128.
42 R. Su, H. A. Hsain, M. Wu, D. Zhang, X. Hu, Z. Wang, X. Wang, F.-T. Li, X. Chen, L. Zhu, Y. Yang, Y. Yang, X. Lou and S. J. Pennycook, *Angew. Chem., Int. Ed.*, 2019, **58**, 15076–15081.
43 Y. Zhang, Y.-M. Sun, X. Ren, J. Hu, H.-J. Yu, J.-G. Liu, H.-W. Huang and J. Han, *Angew. Chem., Int. Ed.*, 2025, **64**, e202416221.
44 P.-X. Zhang, Q. Li, R. Su, H.-Y. Wang, X.-M. Shi, S.-Q. Deng, Y. Bai, H. Zeng, X.-X. Yu, Z.-G. Li, H. Wu, F. Xue, M.-X. Lv, C.-Y. Yu, Y.-L. Cao, X. Chen, J.-X. Deng, J. Miao, K. Lin and X.-R. Xing, *J. Am. Chem. Soc.*, 2025, **147**, 12012–12023.
45 X.-H. Wang, X. Zhang, X. He, G. Guo, Q. Huang, F. You, Q. Wang, R. Qu, F. Zhou and Z. Lian, *Angew. Chem., Int. Ed.*, 2024, **63**, e202410334.
46 X. Wang, X. Zhang, L. Xue, Q. Wang, F. You, L. Dai, J. Wu, S. Kramer and Z. Lian, *Angew. Chem., Int. Ed.*, 2023, **62**, e202307054.
47 Y.-D. Pang, J.-W. Lee, K. Kubota and H. Ito, *Angew. Chem., Int. Ed.*, 2020, **59**, 22570–22576.
48 K. Kubota, Y. D. Pang, A. Miura and H. Ito, *Science*, 2019, **366**, 1500–1504.
49 R. Qu, S. Wan, X. Zhang, X. Wang, L. Xue, Q. Wang, G.-J. Cheng, L. Dai and Z. Lian, *Angew. Chem., Int. Ed.*, 2024, **63**, e202400645.
50 Q. Pan, Z.-X. Gu, R.-J. Zhou, Z.-J. Feng, Y.-A. Xiong, T.-T. Sha, Y.-M. You and R.-G. Xiong, *Chem. Soc. Rev.*, 2024, **53**, 5781–5861.
51 H.-Y. Liu, H.-Y. Zhang, X.-G. Chen and R.-G. Xiong, *J. Am. Chem. Soc.*, 2020, **142**, 15205–15218.
52 C.-R. Huang, X. Luo, X.-G. Chen, X.-J. Song, Z.-X. Zhang and R.-G. Xiong, *Natl. Sci. Rev.*, 2021, **8**, nwaa232.
53 H.-Y. Zhang, Y.-Y. Tang, Z.-X. Gu, P. Wang, X.-G. Chen, H.-P. Lv, P.-F. Li, Q. Jiang, N. Gu, S. Ren and R.-G. Xiong, *Science*, 2024, **383**, 1492–1498.
54 C. Shi, J.-J. Ma, J.-Y. Jiang, M.-M. Hua, Q. Xu, H. Yu, Y. Zhang and H.-Y. Ye, *J. Am. Chem. Soc.*, 2020, **142**, 9634–9641.
55 J. Harada, H. Takahashi, R. Notsuka, M. Takehisa, Y. Takahashi, T. Usui and H. Taniguchi, *Angew. Chem., Int. Ed.*, 2023, **62**, e202215286.
56 Y.-H. Fang, Z. Liu, S. Zhou, P.-X. Fu, Y.-X. Wang, Z.-Y. Wang, Z.-M. Wang, S. Gao and S.-D. Jiang, *J. Am. Chem. Soc.*, 2022, **144**, 8605–8612.
57 W.-F. Deng, Y.-X. Li, Y.-X. Zhao, J.-S. Hu, Z.-S. Yao and J. Tao, *J. Am. Chem. Soc.*, 2023, **145**, 5545–5552.
58 S.-G. Han, J. Bie, W. Fa, S. Chen, L. W. Tang, W.-Q. Guo, H.-J. Xu, Y. Ma, Y. Liu, X.-T. Liu, Z.-H. Sun and J.-H. Luo, *J. Am. Chem. Soc.*, 2024, **146**, 8298–8307.
59 H.-H. Chen, H. Peng, Z.-K. Xu, X.-J. Song, X.-G. Chen, R.-G. Xiong and W.-Q. Liao, *J. Am. Chem. Soc.*, 2025, **147**, 10715–10723.
60 S. Sahoo, S. Mukherjee, V. B. Sharma, W. I. Hernández, A. C. Garcia-Castro, J. K. Zareba, D. Kabra, G. Vaitheeswaran and R. Boomishankar, *Angew. Chem., Int. Ed.*, 2024, **63**, e202400366.
61 Y. Hu, L. You, B. Xu, T. Li, S. A. Morris, Y. Li, Y. Zhang, X. Wang, P.-S. Lee, H.-J. Fan and J. Wang, *Nat. Mater.*, 2021, **20**, 612–617.
62 T.-M. Guo, F.-F. Gao, Y.-J. Gong, Z.-G. Li, F. Wei, W. Li and X.-H. Bu, *J. Am. Chem. Soc.*, 2023, **145**, 22475–22482.
63 J. Long, M. S. Ivanov, V. A. Khomchenko, E. Mamontova, J.-M. Thibaud, J. Rouquette, M. Beaudhuin, D. Granier, R. A. S. Ferreira, L. D. Carlos, B. Donnadieu, M. S. C. Henriques, J. A. Paixão, Y. Guari and J. Larionova, *Science*, 2020, **367**, 671–676.
64 X.-J. Song, W. Sun, L.-X. Zhou, W.-X. Mao, H.-M. Xu, J.-F. Lan, Y. Zhang and H.-Y. Zhang, *J. Am. Chem. Soc.*, 2024, **146**, 32519–32528.
65 H.-H. Hu, Z.-Y. Jing, Q. Pan, T.-T. Sha, H.-R. Ji, X.-X. Cao, X.-J. Song, Z.-J. Feng, J. Yao, R.-J. Zhou, C. Wang, R.-G. Xiong and Y.-M. You, *Adv. Mater.*, 2024, **36**, 2413547.
66 J.-C. Qi, H. Peng, Z.-K. Xu, Z.-X. Wang, Y.-Y. Tang, W.-Q. Liao, G.-F. Zou, Y.-M. You and R.-G. Xiong, *Nat. Commun.*, 2024, **15**, 6738.
67 L.-T. Li, C. Wang, C.-R. Huang, W.-Q. Liao, X.-L. Xu, L.-B. Xiao, R.-N. Wang, W.-Y. Cheng, T.-W. He, S. Cong, Z.-H. Kang, R.-G. Xiong and G.-F. Zou, *J. Am. Chem. Soc.*, 2025, **147**, 12635–12643.
68 J.-C. Qi, X.-J. Song, H. Peng, X.-G. Chen, R.-G. Xiong and W.-Q. Liao, *Adv. Funct. Mater.*, 2025, **35**, 2502822.
69 H.-H. Hu, R. Liu, Y.-B. Zhu, T.-T. Sha, X.-X. Cao, Z.-J. Feng, H.-R. Ji, Q. Pan, R.-G. Xiong and Y.-M. You, *Angew. Chem., Int. Ed.*, 2025, **64**, e202500176.
70 Z.-N. Zhou, Q.-D. Chong, Y.-W. Yang, Z.-W. Hu, W. Ren, S.-S. Zhang and Q. Ye, *Angew. Chem., Int. Ed.*, 2025, **64**, e202510596.
71 H. Zheng, A. Ghosh, M. J. Swamynadhan, Q. Zhang, W. P. D. Wong, Z. Wu, R. Zhang, J. Chen, F. Cimpoesu, S. Ghosh, B. J. Campbell, K. Wang, A. Stroppa, R. Mahendiran and K. P. Loh, *Nat. Commun.*, 2024, **15**, 5556.
72 A.-O. Polyakov, A.-H. Arkenbout, J. Baas, G.-R. Blake, A. Meetsma, A. Caretta, P.-H. M. van Loosdrecht and T. T. M. Palstra, *Chem. Mater.*, 2012, **24**, 133–139.
73 B. Kundys, A. Lappas, M. Viret, V. Kapustianyk, V. Rudyk, S. Semak, Ch. Simon and I. Bakaimi, *Phys. Rev. B*, 2010, **81**, 224434.
74 Y.-X. Dou, X.-M. Wang, N. W. G. Smith, P. Behera, R.-H. Mudiyanselage, B. Guzelturk, D. A. Walko, Y. Pleimling, S.-H. Liu, N. Nici, C. Slebodnick, B. Dryzhakov, B. Hu, A. Raja, R. Ramesh, G. A. Khodaparast, Y.-F. Yan and L.-N. Quan, *Nat. Commun.*, 2025, **16**, 7230.

75 (*a*) CCDC 2484549: Experimental Crystal Structure Determination, 2025, DOI: 10.5517/ccdc.csd.cc2pdcr7; (*b*) CCDC 2484550: Experimental Crystal Structure Determination, 2025, DOI: 10.5517/ccdc.csd.cc2pdcs8; (*c*) CCDC 2484236: Experimental Crystal Structure Determination, 2025, DOI: 10.5517/ccdc.csd.cc2pd1nt; (*d*) CCDC 2484237: Experimental Crystal Structure Determination, 2025, DOI: 10.5517/ccdc.csd.cc2pd1pv; (*e*) CCDC 2484238: Experimental Crystal Structure Determination, 2025, DOI: 10.5517/ccdc.csd.cc2pd1qw; (*f*) CCDC 2484239: Experimental Crystal Structure Determination, 2025, DOI: 10.5517/ccdc.csd.cc2pd1rx; (*g*) CCDC 2484240: Experimental Crystal Structure Determination, 2025, DOI: 10.5517/ccdc.csd.cc2pd1sy; (*h*) CCDC 2484241: Experimental Crystal Structure Determination, 2025, DOI: 10.5517/ccdc.csd.cc2pd1tz; (*i*) CCDC 2484242: Experimental Crystal Structure Determination, 2025, DOI: 10.5517/ccdc.csd.cc2pd1v0; (*j*) CCDC 2484243: Experimental Crystal Structure Determination, 2025, DOI: 10.5517/ccdc.csd.cc2pd1w1; (*k*) CCDC 2484244: Experimental Crystal Structure Determination, 2025, DOI: 10.5517/ccdc.csd.cc2pd1x2; (*l*) CCDC 2484246: Experimental Crystal Structure Determination, 2025, DOI: 10.5517/ccdc.csd.cc2pd1z4; (*m*) CCDC 2484247: Experimental Crystal Structure Determination, 2025, DOI: 10.5517/ccdc.csd.cc2pd206; (*n*) CCDC 2484248: Experimental Crystal Structure Determination, 2025, DOI: 10.5517/ccdc.csd.cc2pd217; (*o*) CCDC 2484249: Experimental Crystal Structure Determination, 2025, DOI: 10.5517/ccdc.csd.cc2pd228; (*p*) CCDC 2484250: Experimental Crystal Structure Determination, 2025, DOI: 10.5517/ccdc.csd.cc2pd239.